Inversion of relative motion data for estimates of the velocity gradient field and fault slip

W. Spakman *

Faculty of Earth Sciences, Utrecht University, Budapestlaan 4, 3584 CD, Utrecht, The Netherlands

M. C. J. Nyst [1]

Delft Institute of Earth Oriented Space Research, Delft University of Technology, Kluyverweg 1, 2629 HS, Delft, The Netherlands

Abstract

A new method is presented for a purely kinematic analysis of relative motion data of crustal deformation. We start by developing a general integral formulation that links the relative motion between two positions to the velocity gradient field. Next, fault slip is explicitly incorporated leading to the final observation equation. This equation provides a new, complete, and in practice, exact description of the time-dependent relation between surface motion and the underlying kinematics. The combination of equations belonging to pairs of observation sites (e.g. of a geodetic network) leads in a natural way to a linear inverse problem from which the velocity gradient field and slip on active faults can be estimated. The method is successfully tested in a synthetic experiment.

Key words: crustal deformation, inversion, relative motion, velocity gradient, strain rate, fault slip

1 Introduction

Relative motions between points at the solid Earth's surface constitute important kinematic boundary conditions for modeling of crustal deformation. For instance, observed motions near active fault zones are often used to constrain certain fault properties [1–3]. In such analysis a popular model for fault behavior is an elastic dislocation embedded in an elastic crust. Dislocation modeling is an example of a more general class of crustal modeling techniques in which observations of surface motion are compared to predictions derived from an assumed physical model of crustal or fault behavior. This implies that resulting kinematic properties, such as the surface flow field and crustal strain rate field, are dependent on the assumptions made. This dependence can be avoided by adopting pure kinematic inversion because in this case knowledge of crustal dynamics and rheology is not required. In a kinematic approach the motion observations are converted into a velocity gradient field and, if possible, estimates of slip on active faults. This provides quantitative information about e.g. the distribution of strain accumulation in the shallow crust and is useful in obtaining qualitative insight into the underlying dynamics. The surface fields obtained from a kinematic analysis, which includes a prediction of the surface velocity-field, can be used as a spatially continuous boundary condition for subsequent dynamic modeling [4].

Kinematic inversion is the subject of this paper. Several inversion methods exist which focus on determining the velocity gradient field $\boldsymbol{\nabla v}(\boldsymbol{r},t)$ from observations of relative crustal motion $\Delta\boldsymbol{v}$. Two classes can be identified: Methods based on interpolation in $\boldsymbol{v}(\boldsymbol{r},t)$-data space and those based on interpolation in $\boldsymbol{\nabla v}(\boldsymbol{r},t)$-model space.

Data space methods first perform a spatial interpolation of the observed $\Delta\boldsymbol{v}$ and next obtain $\boldsymbol{\nabla v}$

* Corresponding author: W. Spakman
Email addresses: wims@geo.uu.nl (W. Spakman), nyst@geo.uu.nl (M. C. J. Nyst).
[1] Now at the U. S. Geological Survey, 345 Middlefield Rd., MS 977, Menlo Park, CA 94025, USA

by spatial differentiation. The interpolation is often based on assuming specific spatial correlations between velocity observations [5–8], but can also be obtained by parameterizing the unknown velocity field by general shape functions of which coefficients are determined by fitting a smooth velocity field to the velocity data [9]. The latter approach is based on earlier data space methods developed for interpolating earthquake derived strain rate data [10], or for a combination of strain rate data and relative motion data [11]. The interpolation methods are derived from geometrical concepts rather than from physical theory relating observations to the velocity gradient field. Contributions of fault motion to observed relative motion are not explicitly incorporated.

Model space methods usually involve a parameterization of the unknown $\boldsymbol{\nabla v}$ field. This is done by shape functions, for instance defined on triangular domains, for which the coefficients are determined in an inversion of the velocity data. Now $\boldsymbol{\nabla v}$ is a direct result of data inversion. Importantly, model space methods are based on a physical theory linking observations with model quantities in terms of an observation equation. Theory in applications has generally been restricted to assuming locally constant $\boldsymbol{\nabla v}$, e.g. in triangular regions spanned by the observation network [12–14]. This leads to velocity gradient fields which are discontinuous across edges of triangles. A velocity gradient field that varies continuously across an entire observation network can been obtained by assuming locally constant $\boldsymbol{\nabla v}$ combined with a prescribed parameter weighting scheme based on distance to observation points [15]. Apart from Lamb [16] we are not aware of any attempt to incorporate fault motion explicitly in a kinematic theory.

In this paper we develop a new kinematic inversion method which in a natural way leads to working in model space. This leads to a generalization and extension of earlier model space approaches. ¿From basic principles we derive an observation equation which relates observations of relative motions to path integrals over the unknown velocity gradient field. The combination of many of such equations leads to an inverse problem for which there is no theoretical restriction on the spatial complexity of the velocity gradient field. In practice, model complexity is determined by the resolving power of the data. A particular novelty is that we also incorporate terms that account for the effects of fault motion on observed relative motions. In the second part of this paper we put the proposed analysis method to the test in a synthetic experiment of crustal deformation.

2 The forward problem

Geodetic observation of crustal deformation yields changes in relative position of points attached to the deforming surface. In a fixed reference frame, adopted at time $t = 0$, the position of a point i is given by $\boldsymbol{r}_i + \boldsymbol{u}(\boldsymbol{r}_i, t)$ where $\boldsymbol{u}$ is the displacement field that evolved since $t = 0$. The relative displacement of a point j with respect to i that developed during time increment $\Delta t = t_2 - t_1$ is: $\Delta \boldsymbol{u}_{ij} = [\boldsymbol{u}(\boldsymbol{r}_j, t_2) - \boldsymbol{u}(\boldsymbol{r}_i, t_2)] - [\boldsymbol{u}(\boldsymbol{r}_j, t_1) - \boldsymbol{u}(\boldsymbol{r}_i, t_1)]$. When $\Delta \boldsymbol{u}_{ij}$ is caused by pure continuous deformation both terms can be related in a general way to the displacement gradient field $\boldsymbol{\nabla u}(\boldsymbol{r}, t)$ by integration at fixed time over arbitrary paths $L_{ij}(t_1)$ and $L_{ij}(t_2)$:

$$\Delta \boldsymbol{u}_{ij} = \int_{L_{ij}(t_2)} \boldsymbol{\nabla u}(\boldsymbol{r}, t_2) \cdot \mathrm{d}\boldsymbol{r} - \int_{L_{ij}(t_1)} \boldsymbol{\nabla u}(\boldsymbol{r}, t_1) \cdot \mathrm{d}\boldsymbol{r} \tag{1}$$

The integration paths can be taken the same in the analysis of short term crustal deformation because the relative error in $\Delta \boldsymbol{u}_{ij}$, due to the mismatch at the endpoints of integration paths, is of the order of $|\boldsymbol{u}(\boldsymbol{r}, t_2) - \boldsymbol{u}(\boldsymbol{r}, t_1)|/l_{ij}$ where l_{ij} is the length of the integration path. This error is usually negligible in the analysis of crustal deformation based on geodetic data. Taking $L_{ij}(t_1) = L_{ij}(t_2)$, $\Delta \boldsymbol{v}_{ij} = \Delta \boldsymbol{u}_{ij}/\Delta t$ and $\Delta \boldsymbol{u} = \boldsymbol{u}(\boldsymbol{r}, t_2) - \boldsymbol{u}(\boldsymbol{r}, t_1)$ equation 1 is rewritten as:

$$\Delta \boldsymbol{v}_{ij} = \int_{L_{ij}} \boldsymbol{\nabla} \left[\frac{\Delta \boldsymbol{u}}{\Delta t} \right] \cdot \mathrm{d}\boldsymbol{r} \tag{2}$$

$\Delta \boldsymbol{v}_{ij}$ is the relative motion derived from repeated geodetic observation of sites i and j. Equation 2 relates $\Delta \boldsymbol{v}_{ij}$ to the linear approximation $\Delta \boldsymbol{u}/\Delta t$ of the crustal flow field $\boldsymbol{v}(\boldsymbol{r}, t) = \mathrm{d}\boldsymbol{u}/\mathrm{d}t$ that developed between t_1 and t_2. If Δt is sufficiently small, as in continuous observation with GPS stations, we get

$$\Delta \boldsymbol{v}_{ij}(t) = \int_{L_{ij}} \boldsymbol{\nabla v}(\boldsymbol{r}, t) \cdot \mathrm{d}\boldsymbol{r} \tag{3}$$

An important property of equation 3 is that it is applicable to time-variable crustal flow. However, this holds only for integration paths that do not cross faults where the $\boldsymbol{\nabla v}$ field can be discontinuous. Effects of fault motion on $\Delta \boldsymbol{v}_{ij}$ can be incorporated by considering the relative motion between two points on the integration path at either

side of a slipping fault (see appendix A). If a path L_{ij} crosses K faults, the relative motion due to fault slip is:

$$\Delta \boldsymbol{v}_{ij}(t) = \sum_{k=1}^{K} \alpha_k \boldsymbol{f}_k(\boldsymbol{r}_{ij}^k, t) \tag{4}$$

where $\boldsymbol{f}_k$ is the slip rate on fault k at time t (or the average slip rate over a period Δt) and occurring at the intersection $\boldsymbol{r}_{ij}^k$ between L_{ij} and the fault. The factor α_k has value +1 or -1 depending on fault orientation with respect to the direction of integration along L_{ij} (see appendix A).

For general crustal flow the combination of equation 3 and 4 relates observed relative motion $\Delta \boldsymbol{v}_{ij}$ to the velocity gradient field and fault slip (figure 1a):

$$\Delta \boldsymbol{v}_{ij} = \sum_{l=1}^{K+1} \int_{L_{ij}^l} \boldsymbol{\nabla v}(\boldsymbol{r}, t) \cdot \mathrm{d}\boldsymbol{r} + \sum_{k=1}^{K} \alpha_k \boldsymbol{f}_k(\boldsymbol{r}_{ij}^k, t) \tag{5}$$

The integration over $\boldsymbol{\nabla v}$ is done in parts because $\boldsymbol{\nabla v}$ can be discontinuous at faults. Equation 5 needs to be extended if $\Delta \boldsymbol{v}_{ij}$ results from two velocity vectors that are taken from independent geodetic networks. In that case an unknown relative rotation between network solutions may exist. The terms to be added to equation 5 are: $\boldsymbol{\Omega}_j \times \boldsymbol{r}_j - \boldsymbol{\Omega}_i \times \boldsymbol{r}_i$ where $\boldsymbol{\Omega}_m$ denotes the rotation vector for the observation network to which site m belongs. One rotation vector can be set to zero in which case the remaining $\boldsymbol{\Omega}_m$ describe the relative rotations with respect to this fixed network. These additional terms are the same as in other kinematic approaches [9,17].

We will use observation equation 5 for the inversion of relative motion data. It has the nice property of being purely linear in the unknown quantities $\boldsymbol{\nabla v}$ and $\boldsymbol{f}_k$. Equation 5 provides a purely kinematic description, hence does not assume anything about crustal or fault dynamics. Most importantly, equation 5 gives a complete description of the relative crustal motion data $\Delta \boldsymbol{v}_{ij}$ resulting from time-variable crustal flow, including coseismic motion. Note that the choice of L_{ij} is completely free. Although this property hints at an inherent non-uniqueness in the interpretation of relative motion data we will turn it to our advantage in the inversion stage.

3 The inverse problem

We restrict our analysis to time independent or time averaged problems and leave non steady motion to future developments. Assume a set of P point positions with known relative motions. These positions yield at least $P(P-1)/2$ vector equations 5 along geodesics or other connecting paths L_{ij} for all combinations of sites i and j. These equations are coupled through the velocity gradient field $\boldsymbol{\nabla v}$ and the relative fault slip rate $\boldsymbol{f}_k$ on fault segments k. In figure 1b this coupling is visualized by the sampling of the surface by integration paths L_{ij}. The resulting inverse problem is to solve this coupled set of integral equations. We note that the forward and inverse problem share strong parallels with those of seismic travel-time tomography (e.g. [18]).

The study region (which can be the entire Earth's surface) is subdivided into a network of N nodes connected by triangulation. The N nodes at the vertices of the triangles need not coincide with observation sites. The only restriction is that triangles cannot intersect with faults. We adopt a linear dependence of $\boldsymbol{\nabla v}$ on the spatial coordinates in each triangle. This parameterization allows for quadratic velocity variation within triangles and continuity of $\boldsymbol{\nabla v}$ across the edges of the triangles. Hence, for each component of the velocity gradient tensor in a particular triangle we assume that

$$[\boldsymbol{\nabla v}(\boldsymbol{r})]_{kl} = \sum_{m=1}^{3} [\boldsymbol{\nabla v}]_{kl}(\boldsymbol{r}_m) g_m(\boldsymbol{r}) \tag{6}$$

where $\boldsymbol{r}_m$ is a vertex of the triangle and $g_m(\boldsymbol{r})$ are interpolation functions. In appendix B we carry this out in more detail. Faults are divided into segments (appendix A) and for each segment k the relative fault slip rate $\boldsymbol{f}_k$ is parameterized as a (segment dependent) constant rate.

Substitution of these parameterizations in 5 leads, after integration, to an ordinary set of coupled linear equations. These can be cast into a matrix-vector form by assembling all velocity gradient parameters into one vector of length $9N$, and by assembling all fault parameters in a vector of length $3K$. Denote these vectors by $\boldsymbol{p}$ and $\boldsymbol{s}$ respectively, then the matrix-vector equivalent of $P(P-1)/2$ vector equations 5 is:

$$[\boldsymbol{V}|\boldsymbol{F}] \begin{bmatrix} \boldsymbol{p} \\ \boldsymbol{s} \end{bmatrix} = \boldsymbol{d} \tag{7}$$

where all data $\Delta \boldsymbol{v}_{ij}$ have been put into one vector $\boldsymbol{d}$. Details of the above steps are presented in appendix B. The submatrix $\boldsymbol{V}$ represents the coefficients linked to continuous deformation, and the non-zero elements of $\boldsymbol{F}$ are +1 or -1 associated with fault segments. It is important to note that going from 5 to 7 only involves the assumptions of linear velocity gradient in triangles and constant slip on fault segments. Higher order parameterizations, e.g. cubic splines, are of course possible and do not affect the principle of the interpretation method we propose here.

The matrix system 7 can be extended with more data equations using the same observation set $\Delta \boldsymbol{v}_{ij}$. For each observation pair i and j many alternative integration paths L_{ij} can be invented which all lead to the same relative motion $\Delta \boldsymbol{v}_{ij}$ (figure 1c). In particular, closed integration paths $L_{ij} - L_{ji}$ between sites i and j will always render zero relative motion. Such equations are welcome because they put constraints on the null space of the inverse problem. If line integration of a continuous vector(tensor) field yields zero for every closed path then the vector(tensor) field is curl-free. We exploit this by requiring that $\boldsymbol{\nabla} \times \boldsymbol{\nabla v} = \boldsymbol{0}$ within each triangle which replaces adding closed-path equations in regions of continuous deforming crust. After substitution of the parameterization (equation 12) this constraint leads to 3 additional equations for each triangle. Additional paths L_{ij} may be required across faults to ensure internal consistency between fault slip and the velocity gradient field. Augmenting 7 with these extra equations leads to:

$$\begin{bmatrix} \boldsymbol{V} & \boldsymbol{F} \\ \boldsymbol{G} & \boldsymbol{0} \end{bmatrix} \begin{bmatrix} \boldsymbol{p} \\ \boldsymbol{s} \end{bmatrix} = \begin{bmatrix} \boldsymbol{d} \\ \boldsymbol{0} \end{bmatrix} \tag{8}$$

where $\boldsymbol{G}$ contains for each triangle the coefficients that result from the constraint $\boldsymbol{\nabla} \times \boldsymbol{\nabla v} = \boldsymbol{0}$.

Data errors cause 8 to be an inconsistent set of equations. These include implicit data errors that may arise from the difference between the spatial variation of true crustal deformation and our parameterized approximation. The implicit errors can be made small by taking sufficiently small triangles and fault segments. In practice, a detailed parameterization combined with a limited amount of data will lead to a mixed-determined or underdetermined inverse problem. To deal with problems associated with data errors, non-uniqueness, and ill-conditioning of the matrix, we adopt an inversion procedure which selects a solution that fits the data best in a least squares sense and at the same time minimizes some model norm. Details can be found elsewhere [19–21]. The following notation is used: $\boldsymbol{A}$ represents the coefficient matrix of equation 8, $\hat{\boldsymbol{d}} = [\boldsymbol{d}|\boldsymbol{0}]^T$, $\boldsymbol{m} = [\boldsymbol{p}|\boldsymbol{s}]^T$, $\boldsymbol{C}_d$ denotes the data covariance matrix, and $\boldsymbol{D}$ stands for a damping or regularization operator that will be specified later. Assuming that the data and model are uncorrelated we choose to minimize the object function: $\Phi(\boldsymbol{m}) = (\boldsymbol{Am} - \hat{\boldsymbol{d}})^T \boldsymbol{C}_d^{-1} (\boldsymbol{Am} - \hat{\boldsymbol{d}}) + \alpha^2 \boldsymbol{m}^T \boldsymbol{D}^T \boldsymbol{Dm}$ where α controls the trade-off between fitting the data and minimizing the weighed model norm. The model $\boldsymbol{m}$ that minimizes Φ is formally: $\boldsymbol{m} = (\boldsymbol{A}^T \boldsymbol{C}_d^{-1} \boldsymbol{A} + \alpha^2 \boldsymbol{D}^T \boldsymbol{D})^{-1} \boldsymbol{A}^T \boldsymbol{C}_d^{-1} \hat{\boldsymbol{d}}$ with a posteriori model covariance given by $\boldsymbol{C} = (\boldsymbol{A}^T \boldsymbol{C}_d^{-1} \boldsymbol{A} + \alpha^2 \boldsymbol{D}^T \boldsymbol{D})^{-1}$ and model resolution kernel $\boldsymbol{R} = \boldsymbol{C} \boldsymbol{A}^T \boldsymbol{C}_d^{-1} \boldsymbol{A}$. The data covariance $\boldsymbol{C}_d$ incorporates the uniform variance σ_r^2 which acts as a row-weight for the exact equations: $\sigma_r^{-1} \boldsymbol{Gp} = \boldsymbol{0}$. Variation of σ_r^{-1} is used to tune the relative importance of these equations with respect to the data equations in determining a solution. In this paper we will work with a combination of amplitude and second derivative regularization. This requires minimizing the object function $\Phi(\boldsymbol{m}) = (\boldsymbol{Am} - \hat{\boldsymbol{d}})^T \boldsymbol{C}_d^{-1} (\boldsymbol{Am} - \hat{\boldsymbol{d}}) + \alpha_a^2 \boldsymbol{m}^T \boldsymbol{m} + \alpha_d^2 \boldsymbol{m}^T \boldsymbol{D}_2^T \boldsymbol{D}_2 \boldsymbol{m}$ where $\boldsymbol{D}_2$ stands for a second derivative operator. The solution that minimizes Φ is

$$\boldsymbol{m} = (\boldsymbol{A}^T \boldsymbol{C}_d^{-1} \boldsymbol{A} + \alpha_a^2 \boldsymbol{I} + \alpha_d^2 \boldsymbol{D}_2^T \boldsymbol{D}_2)^{-1} \boldsymbol{A}^T \boldsymbol{C}_d^{-1} \hat{\boldsymbol{d}} \tag{9}$$

Inversion is now dependent on three tuning parameters: σ_r, α_a and α_d. Target of inversion is a model that can fit the data properly and that has acceptable covariance $\boldsymbol{C}$ and resolution $\boldsymbol{R}$. This requires investigation of a range of solutions obtained for different combinations of the tuning parameters. Of particular importance is the relative weighting between the actual data equations and the additional equations $\sigma_r^{-1} \boldsymbol{Gp} = \boldsymbol{0}$. If σ_r is taken too small the least squares inversion will be dominated by satisfying the latter equations which may lead to a solution with poor fit to the actual data. This is the disadvantage of implementing exact equations as soft constraints.

4 Synthetic experiment

4.1 Design

To create synthetic velocities that are consistent with an underlying crustal deformation field a forward finite-element calculation is performed first.

In spherical geometry a $2^\circ \times 2^\circ$ model area with two frictionless faults is deformed by applying a plane shear stress at the top boundary. The lower boundary is kept fixed and the top, left and right boundaries are free to move. An isotropic elastic rheology is assumed and relative displacements are derived by solving the equation of mechanical equilibrium with the method of [22]. Division of the displacements by an arbitrary time scale of one year leads to the synthetic velocities that become the data for our inverse modeling. Synthetic velocities $\boldsymbol{v} = (v_\theta, v_\phi)$ and strain rates $\dot{\boldsymbol{\epsilon}} = \frac{1}{2}(\boldsymbol{\nabla v} + (\boldsymbol{\nabla v})^T)$ are plotted in figure 2, and fault slip rates $\boldsymbol{f} = (f_\theta, f_\phi)$ in figure 3. The velocity field varies rather smoothly and effects of fault slip rate are not easily recognized in the velocity field displayed. In contrast, the relatively strong variations in strain rate due to the presence of the faults are more striking. We note that in absence of faults the effective strain rate field would be symmetric about the central θ-axis of the model.

We invert the 81 synthetic velocities displayed in figure 2 into estimates of fault slip rate $\boldsymbol{f}$ and the lateral components of velocity gradient field $\boldsymbol{\nabla v}$. The latter is denoted by

$$\boldsymbol{\nabla v} = \begin{bmatrix} v_{\theta\theta} & v_{\theta\phi} \\ v_{\phi\theta} & v_{\phi\phi} \end{bmatrix}.$$

Contributions of the radial derivatives of the lateral components of velocity can be neglected, because in essence we perform a two-dimensional experiment. The inversions are performed on 3 different grids P1, P2 and P3, consisting of 38, 134 and 394 triangles, respectively (figure 4). Fault I(II) consists of 6(8) segments in grids P1 and P2 and of 12(16) segments in grid P3. The spatial domains of the model parameters (triangles and fault segments) are much larger than those used in the forward finite element modeling (see captions of Fig. 2 and 3). Compared to the density of data points grid P3 represents probably the most detailed parameterization one would attempt to use in practice. Consequently, in our test we will not be able to retrieve all details of the synthetic deformation field. In turn, this implies that in general the synthetic data will be inconsistent with (ideal) data predictions from the left hand side of 8. Thus, the signal misfit will act as correlated noise in the inversion. As another link to practice we assume that the synthetic data have been acquired from a geodetic experiment that yielded a uniform observation error of $\sigma_d = 3mm/yr$ on all velocity components.

Weight factors α_a and α_d (equation 9) control the effect of amplitude damping of $\boldsymbol{\nabla v}$, which is applied on boundary nodes only, and of second derivative regularization on all model nodes, respectively. Fault slip parameters are not damped. We compute the inverse matrix of equation 9 by Cholesky decomposition which also provides us with its spectrum of eigenvalues.

We denote the synthetic model with $\boldsymbol{\mu}$. A solution vector $\boldsymbol{m}$ will be expanded on the finite element grid to facilitate comparison with $\boldsymbol{\mu}$. Similar to $\boldsymbol{m}$ the synthetic model consists of two parts; $\boldsymbol{\mu} = [\boldsymbol{p}_\mu \mid \boldsymbol{s}_\mu]^T$, with $\boldsymbol{p}_\mu$ (of length N_c) the components of $(\boldsymbol{\nabla v})_\mu$ and $\boldsymbol{s}_\mu$ (of length N_f) the components of fault slip rate. The total length of model vectors defined on the geometry of the synthetic model is $N = N_c + N_f$. The model misfit vector $\boldsymbol{m} - \boldsymbol{\mu}$ is split into $\boldsymbol{\delta p}_\mu = \boldsymbol{p}_\mu - \boldsymbol{p}_m$ and $\boldsymbol{\delta s}_\mu = \boldsymbol{s}_\mu - \boldsymbol{s}_m$.

For the analysis of the inversion results we define a root-mean-square misfit function $\Psi_I(\boldsymbol{x}, \boldsymbol{y}) = \|\boldsymbol{x} - \boldsymbol{y}\|/\|\boldsymbol{x}\|$ for comparison of vectors of length I. Thus, the model misfit is $\Psi_N(\boldsymbol{\mu}, \boldsymbol{m})$. Misfit is also computed separately for the two parts of the model: $\Psi_{N_c}(\boldsymbol{p}_\mu, \boldsymbol{p}_m)$ and $\Psi_{N_f}(\boldsymbol{s}_\mu, \boldsymbol{s}_m)$, respectively. Data misfit is given by $\Psi_M(\boldsymbol{d}, \boldsymbol{d}_m)$ which compares the synthetic data $\boldsymbol{d}$ with predicted data $\boldsymbol{d}_m$. M includes the $81(81-1)$ data constraints plus the number of equations of the $\sigma_r^{-1}\boldsymbol{Gp} = \boldsymbol{0}$ constraint. The latter adds two equations per triangle. We also compute the usual model correlation coefficients $\rho(\boldsymbol{\mu}, \boldsymbol{m}) = \boldsymbol{\mu} \cdot \boldsymbol{m}/(\|\boldsymbol{\mu}\| \cdot \|\boldsymbol{m}\|)$.

4.2 Inversion results

Some input and output parameters belonging to inversions on each grid are listed in table 1. The Ψ-measures for model and data misfit belong to the preferred solutions on each grid which were obtained by scanning a wide range in each of the three tuning parameters [23]. Preferred solutions have minima in $\Psi_N(\boldsymbol{\mu}, \boldsymbol{m})$ and $\Psi_M(\boldsymbol{d}, \boldsymbol{d_m})$ for more or less similar values of the damping parameters. The minimum in the data misfit $\Psi_M(\boldsymbol{d}, \boldsymbol{d_m})$ is constrained to be in accord with the adopted uniform data noise of $3mm/yr$. Figure 5 shows the influence on normalized spectra of $\boldsymbol{C}^{-1}$ of adding extra constraints (in the form of $\boldsymbol{\nabla} \times \boldsymbol{\nabla v} = \boldsymbol{0}$ and damping). Many of the small eigenvalues are associated with eigenvectors pertaining to fault slip and, as we will infer later, trade-off between fault slip and $\boldsymbol{\nabla v}$ as a result of lack of resolution. The extra constraints represented by $\sigma_r^{-1}\boldsymbol{Gp} = \boldsymbol{0}$ considerably lower the spectra (dashed lines in figure 5) by factors of about 2, 20, and 200 on the grids P1, P2 and P3, respectively. The values

of σ_r were tuned to render an acceptable fit to the actual relative motion data. Thus, these extra constraints considerably improve the conditioning of the inverse problem. Still, additional damping proved necessary to control solution contributions from the low end of the spectrum. This reduces the roughness of the solution and still renders the data misfit in accord with the imposed noise level. From table 1 we also infer a general improvement of model and data fit for increasing density of the parameterization. Further, the model correlation coefficient $\rho(\boldsymbol{\mu}, \boldsymbol{m})$ is generally high and ranges between 0.87 (P1) and 0.97 (P3) for $\boldsymbol{s}$ and between 0.95 (P1) and 0.98 (P3) for $\boldsymbol{p}$. We note that the overparameterization of P3 with respect to station density still improves the model fit. This shows that placing model nodes at station positions only (experiment on grid P2) can be a too conservative choice of parameterization.

Only on grid P3 we obtain minimal values of data and model misfit for similar values of the damping parameters. This model is obtained for $\sigma_r = \sigma_r^\mu$, $\alpha_a = \alpha_a^\mu$ and $\alpha_d = \alpha_d^\mu$ (see table 1). The solution is plotted in figure 6 (panels (b)) and in general compares well with the synthetic model (panels (a)). We infer three different types of misfit patterns (panels (c)). First, the largest part of $\Psi_{N_c}(\boldsymbol{p}_\mu, \boldsymbol{p}_m)$ is caused by the small-scale, but large amplitude, misfit near fault tips. Apparently, the model parameterization is still too coarse to accommodate these variations. However, further densification of the triangular grid proved of no use, because the local variations near the fault tips are not sufficiently detected by the observation network. Second, we find model misfits of somewhat smaller magnitude surrounding the faults. Part of these patterns vary linearly over the triangles and correlate with the slip misfit vectors $\boldsymbol{\delta s}_\mu$ (figure 6.3c). For instance, a slight overestimation of the thrusting component on fault II is compensated by extension near the fault (figure 6.2c). The trade-off can best be limited by placing additional stations along the faults which demonstrates that the trade-off is predominantly due to lack of data and to a much lesser extend is forced by the coarseness of the model parameterization [23]. The third source for misfit is represented by relatively long-wavelength patterns of alternating positive and negative amplitude. Path integration over these misfit patterns yields zero or near-zero relative velocity which demonstrates their closeness to the null space. This effect is similar to that observed in synthetic travel-time tomography experiments [24] where geometrical symmetry in the experiment design caused zero eigenvalues with associated eigenvectors possessing large-scale variation (i.e. with respect to the detail of parameterization).

We find that the predominant part of the model misfit is contained within the bounds imposed by the model errors for $\boldsymbol{\nabla v}$ (figure 7). Only in narrow zones along the model boundaries and along the faults the model misfit for $\boldsymbol{\nabla v}$ exceeds the model errors. For the fault slip the misfit exceeds the model errors by on average 2 to 3 mm/yr. An increase of the adopted data error to $6mm/yr$ would remedy this situation. However, it is more important to acknowledge that true model errors can exceed the formal error as a result of solution trade-off caused by lack of data and by correlated data noise not accounted for by the data covariance matrix.

Figure 8 shows the diagonal components R_{ii} of the resolution kernel $\boldsymbol{R}$ and C_{ii} of the model covariance $\boldsymbol{C}$, The $v_{\theta\theta}$ and $v_{\phi\theta}$ components have equal resolution and are in general better resolved than the $v_{\theta\phi}$ (and $v_{\phi\phi}$) components and exhibit smaller covariance. A similar observation is made for fault II with respect to fault I, of which the latter accommodates mostly ϕ-oriented fault slip. Less well resolved model parameters with relatively large model errors are located along the faults, reflecting the inferred solution trade-off, and along the boundaries of the model area where the baseline sampling is poorer than in the interior of the model.

5 Discussion and conclusions

The synthetic data for our experiments where constructed to be internally consistent with the synthetic deformation field. Further, to mimic data complexities of real data sets the synthetic model possessed more detail than could be resolved with the parameterization adopted. The synthetic experiment demonstrates that our proposed kinematic inversion method works well to obtain joint estimates of the velocity gradient field and slip rate on active faults. Additional constraints in the form of $\boldsymbol{\nabla} \times \boldsymbol{\nabla v} = \boldsymbol{0}$ data equations improve the conditioning of the inverse problem and increase the model fit. Model misfit patterns could be sufficiently minimized by increasing the density of parameterization. Remaining misfit patterns could basically be understood as a result of (the imposed) lack of data.

The only basic problem we encountered is the trade-off between fault slip and the velocity gradient field. We stress that this effect is due to lack of data. Any inversion method of relative motions

will one way or another encounter this problem and have to deal with it. Our method offers sufficient flexibility to study trade-off phenomena. For instance, inversion can be restricted to solving for the velocity gradient only which leads to a test of the hypothesis that all faults are essentially locked at the surface. Similarly, one can test the hypothesis that the velocity gradient is zero and that fault slip purely reflects crustal block motion. The trade-off may complicate the interpretation of estimated fault slip in inversions of real data. If only observation sites are used far away from faults, the estimated fault slip will reflect predominantly (long term) crustal block motion, i.e. independent of fault locking. If sites are used close to faults, the actual fault motion will prevail in the estimate which includes obtaining zero motion if a fault has been locked during the observation period. Using observation sites close to faults is the only remedy (for any method) to break the trade-off.

With regard to a comparison with existing interpretation techniques (see section 1) we note that our proposed method completely generalizes earlier developments in model space approaches. In contrast to data-space interpolation techniques our model space approach is explicitly based on a general and valid physical relation between observations and the underlying kinematic fields. Further, it includes the contributions of slipping faults to observed crustal flow.

One interesting development would be to include time as an independent parameter in the inversion and invert time series obtained from permanent observation with GPS. We foresee no conceptional problems for this application because time is already included in the observation equation (equation 5). In areas with high seismicity this application would allow to map the spatial and temporal development of the velocity gradient field and fault slip which includes elastic fault loading, coseismic motion, and postseismic relaxation. We leave this for future development.

Concluding, we developed and tested a new kinematic analysis method to simultaneously estimate the velocity gradient field and fault slip from an inversion of relative motion data. The method is based on first principles of kinematic deformation and (in theory) applicable to general short-term time-variable crustal flow. The observation equation 5 provides a complete description of the kinematic contributions to relative motion. The quality of estimated quantities is primarily determined by the quality of the data and to a lesser extent depends on the few assumptions underlying model parameterization. The proposed method is independent of spatial scale and can be applied to local deformation problems or studies of global crustal deformation and plate motion.

Acknowledgements

We are endebted to Rob Govers for the computation of the synthetic finite element model. We benefited from many stimulating discussions with Rinus Wortel, Rob Govers, and Boudewijn Ambrosius. We thank Hans-Gert Kahle and an anonymous reviewer for their constructive comments. The model triangulation was made with a program by Shewchuk [25]. This work was conducted under the research programmes of the Vening Meinesz Research School of Geodynamics (VMSG) and the Netherlands Research Centre for Integrated Solid Earth Sciences (ISES).

6 Appendix A: Fault motion and fault parameterization

Consider an arbitrary integration path L_{ij} crossing a fault in a deforming medium. We parameterize L_{ij} with the arc-length parameter l and take $l = 0$ at the intersection of L_{ij} with the fault. The integration 3 is split into three parts:

$$\Delta \boldsymbol{v}_{ij} = \int_{l_i}^{-\epsilon} \boldsymbol{\nabla v} \cdot \frac{d\boldsymbol{r}}{dl} \mathrm{d}l + \int_{-\epsilon}^{+\epsilon} \frac{d\boldsymbol{v}}{dl} \mathrm{d}l + \int_{+\epsilon}^{l_j} \boldsymbol{\nabla v} \cdot \frac{d\boldsymbol{r}}{dl} \mathrm{d}l \qquad (10)$$

where ϵ is a small arc distance. The second term on the right hand side reduces to $\boldsymbol{v}(+\epsilon) - \boldsymbol{v}(-\epsilon)$ which is the difference in velocity across the fault over an interval 2ϵ. If the fault is locked and $\epsilon \to 0$ this term vanishes because of the continuity of $\boldsymbol{v}$. To simulate a slip rate on the fault we let $\boldsymbol{v}$ depend on ϵ and generate a sequence of differentiable velocity functions $\boldsymbol{v}_\epsilon(l)$ which converge to $\boldsymbol{v}$ when $\epsilon \to 0$. Since the fault is slipping the velocity profiles $\boldsymbol{v}_\epsilon$ converge to a step function at the fault with $\boldsymbol{v}(-\epsilon) \to \boldsymbol{v}(0^-)$ and $\boldsymbol{v}(+\epsilon) \to \boldsymbol{v}(0^+)$. Substituting $\boldsymbol{v}_\epsilon$ for $\boldsymbol{v}$ in equation 10 and letting $\epsilon \to 0$ reduces the second term on the right hand side to nonvanishing fault slip rate while integration in the first term ends at the fault at $l = 0^-$ and in the last term integration starts at $l = 0^+$. This leads to the addition of path integration and faults slip-rate terms which, after defining sign conventions, leads to equation 5.

The sign α_k of the fault slip term in equation 4 depends on the direction of integration. To develop a consistent way of adding fault slip terms we first define the parameterization of fault geometry and relative sense of fault motion. Fault geometry is parameterized on the Earth surface as straight (or great circle) fault segments connected by support points $\boldsymbol{r}_k, k = 1, 2, ..$ (figure 9a, b). Let $\boldsymbol{T}_k = (\boldsymbol{r}_{k+1} - \boldsymbol{r}_k)/|\boldsymbol{r}_{k+1} - \boldsymbol{r}_k|$ denote the tangential unit vector of a segment, then the unit normal $\boldsymbol{N}_k$ on the segment is taken at 90 degrees counterclockwise from $\boldsymbol{T}_k$. The upward pointing unit vector is denoted by $\boldsymbol{B}_k$. We label the two crustal blocks separated by a fault segment as block 1 and block 2 where $\boldsymbol{N}_k$ always points into block 1. Let $\Delta\boldsymbol{s}_k^1$ and $\Delta\boldsymbol{s}_k^2$ represent the absolute 3-D block displacement of block 1 and 2, respectively. We define the relative fault slip as: $\Delta\boldsymbol{s}_k = \Delta\boldsymbol{s}_k^1 - \Delta\boldsymbol{s}_k^2$ which gives the relative displacement of block 1 with respect to block 2. This definition is completely determined by $\boldsymbol{T}_k$ and changes sign if $\boldsymbol{T}_k$ is reversed in direction. However, the sense of relative displacement is preserved independent of the direction of $\boldsymbol{T}_k$. Let Δs_k^T, Δs_k^N and Δs_k^B denote the projections of $\Delta\boldsymbol{s}_k$ on the three unit vectors. Right lateral displacement is given by $\Delta s_k^T > 0$, left lateral displacement by $\Delta s_k^T < 0$, normal faulting by $\Delta s_k^N > 0$, and thrusting by $\Delta s_k^N < 0$. Note that $\Delta\boldsymbol{s}_k$ also fixes the fault dip.

When an integration path crosses K faults the total fault slip contribution to relative motion generalizes to equation 4 where $\alpha_k = sign(\boldsymbol{N}_k \cdot \boldsymbol{l}_{ij})$ and $\boldsymbol{l}_{ij}$ the local tangent to L_{ij} in the direction of integration. In 4 $\boldsymbol{f}_k$ denotes the fault slip rate which represents either a time average of fault slip $\Delta\boldsymbol{s}_k/\Delta t$ or approximates the true rate (fault creep rate or coseismic velocity) depending on the time elapsed between observations of relative motion.

7 Appendix B: Parameterization of $\nabla\boldsymbol{v}$

The parameterization of $\nabla\boldsymbol{v}$ is restricted to specifying its spatial behavior for each single triangle T^τ by shape functions. Let L^τ denote the path segment in T^τ of an integration path L (where we dropped the subscript ij to save on notation). Then equation 3 can be written as:

$$\Delta\boldsymbol{v} = \sum_\tau (\Delta\boldsymbol{v})^\tau = \sum_\tau \int_{L^\tau} \nabla\boldsymbol{v}(\boldsymbol{r}) \cdot \mathrm{d}\boldsymbol{r} \qquad (11)$$

Now we can concentrate on the contribution to $\Delta\boldsymbol{v}$ from one triangle T^τ. The vertices of T^τ correspond to model nodes with position vectors $\boldsymbol{r}_m^\tau, m = 1, 2, 3$. At each vertex m we have 9 model parameters assembled in $\nabla\boldsymbol{v}(\boldsymbol{r}_m^\tau)$. We denote the kl-component (row index k) of $\nabla\boldsymbol{v}(\boldsymbol{r}_m^\tau)$ by $p_{kl}^{\tau m}$, hence in cartesian geometry $p_{kl}^{\tau m} = (\partial v_k/\partial x_l)(\boldsymbol{r}_m^\tau)$. For each component of $\nabla\boldsymbol{v}(\boldsymbol{r})$ the spatial variation in triangle T^τ is determined by:

$$[\nabla\boldsymbol{v}(\boldsymbol{r})]_{kl}^\tau = \sum_{m=1}^{3} p_{kl}^{\tau m} g_m^\tau(\boldsymbol{r}) \qquad (12)$$

where $g_m^\tau(\boldsymbol{r})$ are known functions that interpolate between the unknown model parameters $p_{kl}^{\tau m}$. Substituting this parameterization in the path integral for T^τ gives for the k-th component of $(\Delta\boldsymbol{v})^\tau$:

$$(\Delta\boldsymbol{v})_k^\tau = \int_{L^\tau} [\nabla\boldsymbol{v}(\boldsymbol{r}) \cdot \mathrm{d}\boldsymbol{r}]_k = \sum_{m=1}^{3}\sum_{l=1}^{3} p_{kl}^{\tau m} G_l^{\tau m} \qquad (13)$$

with $G_l^{\tau m} = \int_{\lambda_1}^{\lambda_2} g_m^\tau(\boldsymbol{r}(\lambda))(\frac{\mathrm{d}\boldsymbol{r}(\lambda)}{\mathrm{d}\lambda} \cdot \boldsymbol{q}_l)\mathrm{d}\lambda$, where $\boldsymbol{r}(\lambda) = r_1(\lambda)\boldsymbol{q}_1 + r_2(\lambda)\boldsymbol{q}_2 + r_3(\lambda)\boldsymbol{q}_3, (\lambda_1 < \lambda < \lambda_2)$ parameterizes L^τ with arc length λ. The $\boldsymbol{q}_i$ are unit axis-vectors in the coordinate frame adopted. Except for Cartesian geometry, the $\boldsymbol{q}_i$ may depend on the arc-length parameter λ. Substituting 13 in 11 gives:

$$(\Delta\boldsymbol{v})_k = \sum_\tau \sum_{m=1}^{3}\sum_{l=1}^{3} p_{kl}^{\tau m} G_l^{\tau m} \qquad (14)$$

In the summation over τ, the coefficients $G_l^{\tau m}$ are zero for all triangles T^τ not intersected by path L. Equation 14 can be simplified. Certain combinations of τ and m relate to the same node number n because one node is usually at the vertex of more than one triangle. Therefore, the summation over τ and m can be replaced by a summation over model nodes n yielding

$$(\Delta\boldsymbol{v})_k = \sum_{n=1}^{N}\sum_{l=1}^{3} p_{kl}^n H_l^n \qquad (15)$$

with $H_l^n = \sum_{for"\tau m"=n} G_l^{\tau m}$. In order to arrive at a set of linear equations incorporating all relative motion data we assemble all model parameters into one linear vector $\boldsymbol{p}$ of length $9N$ with $p_j = p_{kl}^n$, $j = l + 3(k-1) + 9(n-1)$. Label the

set of M relative motion vectors (i.e. all relative motion vectors resulting from station combinations including additional closed-path constraints) as $\Delta_\nu \boldsymbol{v}$, $\nu = 1, 2, .., M$ and assemble these into one data vector $\boldsymbol{d}$ of length $3M$ with $d_i = (\Delta_\nu \boldsymbol{v})_k$, $i = k + 3(\nu - 1)$. Equation 15 becomes for all data:

$$d_i = \sum_{j=1}^{9N} V_{ij} p_j \quad i = 1, .., M \tag{16}$$

with $V_{ij} = H_l^n$ or $\boldsymbol{d} = \boldsymbol{V}\boldsymbol{p}$. In cartesian geometry we use linear interpolation functions $g_m^\tau(\boldsymbol{r})$ as for instance given by [26, p. 153]. For straight path segments within triangles the integration of 13 can be performed analytically leading to the coefficients $G_l^{\tau m}$. In spherical geometry a study region is triangulated with spherical triangles. We have adopted (weakly nonlinear) interpolation functions defined by

$$g_m^\tau(\boldsymbol{r}) = [1 - \frac{\mathrm{arc}(\boldsymbol{r}, \boldsymbol{r}_m^\tau)}{\mathrm{arc}(\boldsymbol{r}_m^\tau, \boldsymbol{R}_m^\tau)}] \tag{17}$$

where $\mathrm{arc}(\boldsymbol{r}, \boldsymbol{r}_m^\tau)$ is the arc distance between $\boldsymbol{r}$ and $\boldsymbol{r}_m^\tau$. The point $\boldsymbol{R}_m^\tau$ is located at the triangle side facing node $\boldsymbol{r}_m^\tau$ at the intersection with the great circle arc spanned by $\boldsymbol{r}_m^\tau$ and $\boldsymbol{r}$. Integration is performed numerically.

We remark that all numbers 3 and 9 in this appendix change to 2 and 4, respectively, if we would consider a two-dimensional problem.

References

[1] J.C. Savage and R.O. Burford, Geodetic determination of relative plate motion in central California, *J. Geophys. Res.* **78** (1973) 832–845.

[2] M. Matsu'ura, D.D. Jackson and A. Cheng, Dislocation model for aseismic crustal deformation at Hollister, California, *J. Geophys. Res.* **91** (1986) 12,661–12,674.

[3] J.F. Genrich, Y. Bock, R. McCaffrey, L. Prawirodirdjo, C.W. Stevens, S.S.O Puntodewo, C. Subarya and S. Wdowiski, Distribution of slip at the northern Sumatran fault system, *J. Geophys. Res.* **105** (2000) 28,327–28,341.

[4] L. Flesch, A.J. Haines, W.E. Holt, Dynamics of the India-Eurasia collision zone, *J. Geophys. Res.* **106** (2001) 16,435–16,460.

[5] Ch. Straub, Recent Crustal Strain Accumulation in the Marmara Sea Region, NW Anatolia, inferred from GPS Measurements, *PhD Dissertation* (Eidgenössischen Technischen Hochschule, Zürich, 1996).

[6] T. Kato, G.S. El-Fiky, E.N. Oware and S. Miyazaki, Crustal strains in the Japanese island as deduced from dense GPS arrays, *Geophys. Res. Lett.* **25** (1998) 3445–3449.

[7] S.N. Ward, On the consistency of earthquake moment rates, geological fault data, and space geodetic strain: the United States, *Geophys. J. Int.* **134** (1998) 172–186.

[8] H.-G. Kahle, M. Cocard, Y. Peter, A. Geiger, R. Reilinger, A. Barka and G. Veis, GPS-derived strain rate field within the boundary zones of the Eurasian, African, and Arabian Plates, *J. Geophys. Res.* **105** (2000) 23,353–23,370.

[9] J. Beavan and J. Haines, Contemporary horizontal velocity and strain rate fields of the Pacific-Australian plate boundary zone through New Zealand, *J. Geophys. Res.* **106** (2001) 741–770.

[10] A.J. Haines and W.E. Holt, A procedure for obtaining the complete horizontal motions within zones of distributed deformation from the inversion of strain data, *J. Geophys. Res.* **98** (1993) 12,057–12,082.

[11] B. Shen-Tu, W.E. Holt and A.J. Haines, Deformation kinematics in the western United States determined from Quaternary fault slip rates and recent geodetic data, *J. Geophys. Res.* **104** (1999) 28,927–28,955.

[12] F.C. Frank, Deduction of Earth strains from survey data, *Bull. Seismol. Soc. Am.* **56** (1966) 35–44.

[13] R.R. Davies, P. England, B. Parsons, H. Billiris, D. Paradissis and G. Veis, Geodetic strain of Greece in the interval 1892-1992, *J. Geophys. Res.* **102** (1997) 24,571–24,588.

[14] S.J. Bourne, T. Árnadóttir, J. Beavan, D.J. Darby, P.C. England, B. Parsons, R.I. Walcott and P.R. Wood, Crustal deformation of the Marlborough fault zone in the South Island of New Zealand: Geodetic constraints over the interval 1982-1994, *J. Geophys. Res.* **103** (1998) 30,147–30,165.

[15] Z.-K. Shen, D.D. Jackson, and B.X. Ge, Crustal deformation across and beyond the Los Angeles basin from geodetic measurements, *J. Geophys. Res.* **101** (1996) 27,957–27,980.

[16] S.H. Lamb, Behavior of the brittle crust in wide plate boundary zones, *J. Geophys. Res.* **99** (1994) 4457–4483.

[17] C. Kreemer, W.E. Holt, S. Goes, and R. Govers, Active deformation in eastern Indonesia and the Philippines from GPS and seismicity data, *J. Geophys. Res.* **105** (2000) 663–680.

[18] H. Bijwaard, W. Spakman, and E.R. Engdahl, Closing the gap between regional and global travel time tomography, *J. Geophys. Res.* **103** (1998) 30,055–30,078.

[19] D.D. Jackson, The use of a priori data to resolve non-uniqueness in linear inversion, *Geophys. J. R. Astron. Soc.* **57** (1979) 137–157.

[20] W.Menke, *Geophysical Data Analysis: Discrete Inverse Theory (revised edition)* (International Geophysics Series, Academic Press Inc., San Diego, USA, 1989).

[21] J.A. Scales, P. Docherty and A. Gerztenkorn, Regularisation of non-linear inverse problems: imaging the near-surface weathering layer, *Inverse Problems* **6** (1990) 115–131.

[22] R.M.A. Govers, Dynamics of lithospheric extension: A modeling study, *Ph.D. Dissertation* (Utrecht University, The Netherlands, 1993).

[23] M.C.J. Nyst, A new approach to model the kinematics of crustal deformation, with applications to the Aegean and Southeast Asia, *Ph.D. dissertation* (Delft University of Technology, Delft, The Netherlands, 2001).

[24] J.-J. Lévêque, L. Rivera and G. Wittlinger, On the use of the checker-board test to assess the resolution of tomographic inversions, *Geophys. J. Int.* **115** (1993) 313–318.

[25] J. Shewchuk, Triangle: Engineering a 2D quality mesh generator and Delaunay triangulator, *First workshop on applied computational geometry* (Pennsylvania, 1996).

[26] D.C. Cook, D.S. Malkus and M.E. Plesha, *Concepts and applications of finite element analysis* (John Wiley & Sons, New York, 1989).

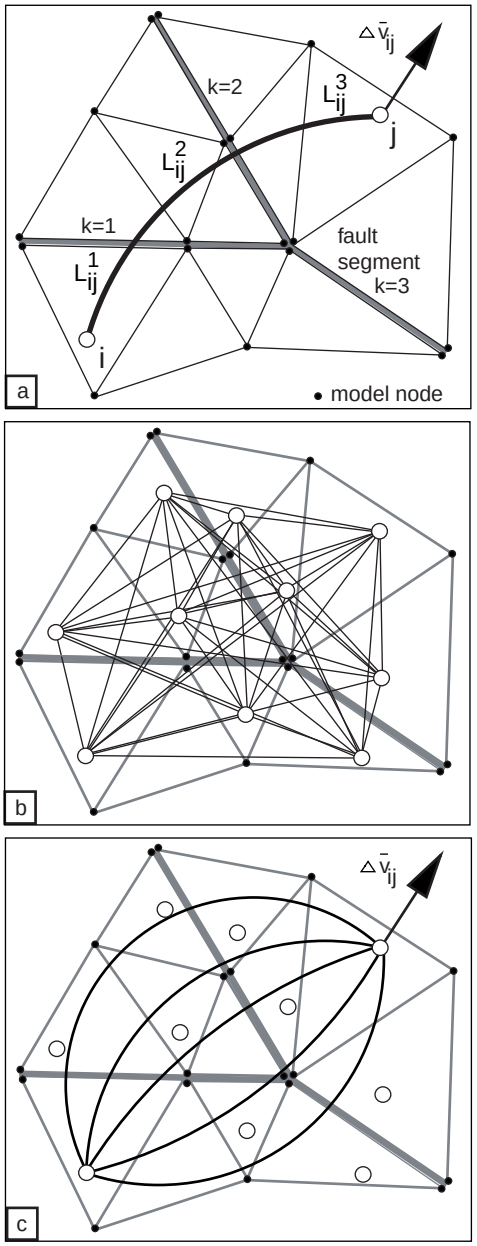

Fig. 1. Schematic representation of model geometry: a) A study region with a "Y"-shape fault system is triangulated between model nodes (black dots). Triangles do not intersect faults. Nodes at the fault are doubled to allow the velocity gradient field to be discontinuous across faults. The curved path L_{ij} connects two observation sites i and j with relative motion $\Delta \boldsymbol{v}_{ij}$. b) Ten observation sites (open circles) are connected by 45 geodesics, yielding 135 component equations in the forward problem. c) For observation sites at opposite sides of faults extra path equations (denoted by curved lines) can be included to force internal consistency between fault slip and the velocity gradient field in the inversion.

Table 1
Parameters for inversion for $\nabla \boldsymbol{v}$ and $\boldsymbol{s}$.

grid	T_n	T_t	σ_r^μ	$\tilde{\sigma}_p^\mu$	$\tilde{\sigma}_s^\mu$	Ψ_{N_c}	Ψ_{N_f}	Ψ_M
			$\frac{1}{myr}$	$[\frac{1}{yr}]$	$[\frac{m}{yr}]$	%	%	%
P1	32	38	$1.4{\cdot}10^{-12}$	$1{\cdot}10^{-8}$	0.004	23	30	3.5
P2	88	134	$2.1{\cdot}10^{-12}$	$3{\cdot}10^{-8}$	0.001	21	26	2. 5
P3	218	394	$4.6{\cdot}10^{-12}$	$4{\cdot}10^{-8}$	0.0008	17	20	2

Key for the input parameters: T_n, number of grid nodes; T_t, number of triangles; and σ_r^μ, the standard deviation for $\boldsymbol{G}$. Key for the output parameters: $\tilde{\sigma}_p^\mu$, $\tilde{\sigma}_s^\mu$ average model standard deviation for components of $\nabla \boldsymbol{v}$, $\boldsymbol{s}$, respectively; Ψ_{N_c}, Ψ_{N_f}, model misfit for velocity gradient parameters, slip parameters, and Ψ_M the data misfit.

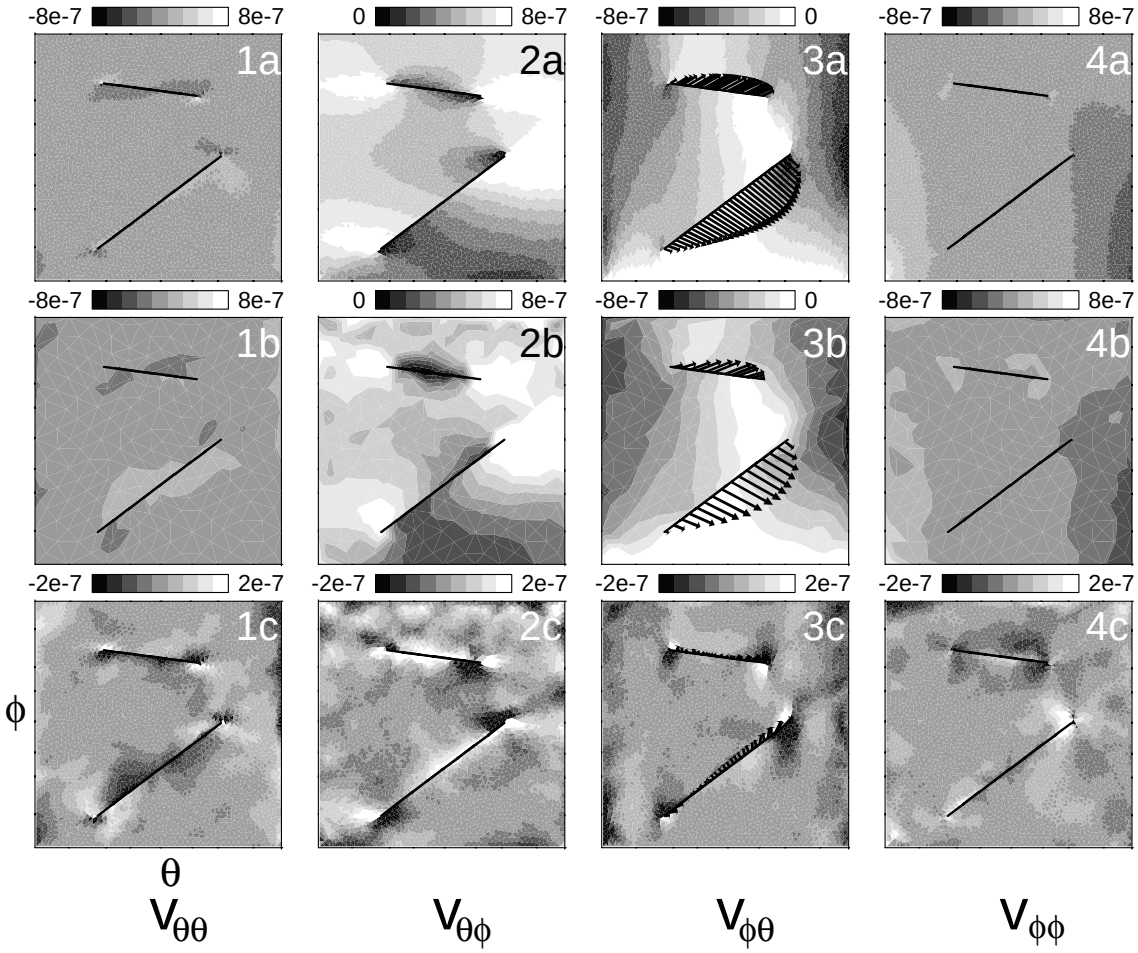

Fig. 6. Selected solution $\boldsymbol{m}$ on grid P3. The contouring (note the different scales) displays each of the components of $\nabla \boldsymbol{v}$ in units yr^{-1}. The top panels show the exact synthetic model $\boldsymbol{p}_\mu$. The central panels show the preferred solution $\boldsymbol{p}_m$, and the bottom panels show the difference $\delta \boldsymbol{p}_\mu = \boldsymbol{p}_\mu - \boldsymbol{p}_m$. The faults slip is plotted in the third column. From top to bottom: (3a) synthetic slip $\boldsymbol{s}_\mu$; (3b) the inversion result $\boldsymbol{s}_m$, and (3c) the misfit $\boldsymbol{\delta s}_\mu = \boldsymbol{s}_\mu - \boldsymbol{s}_m$.

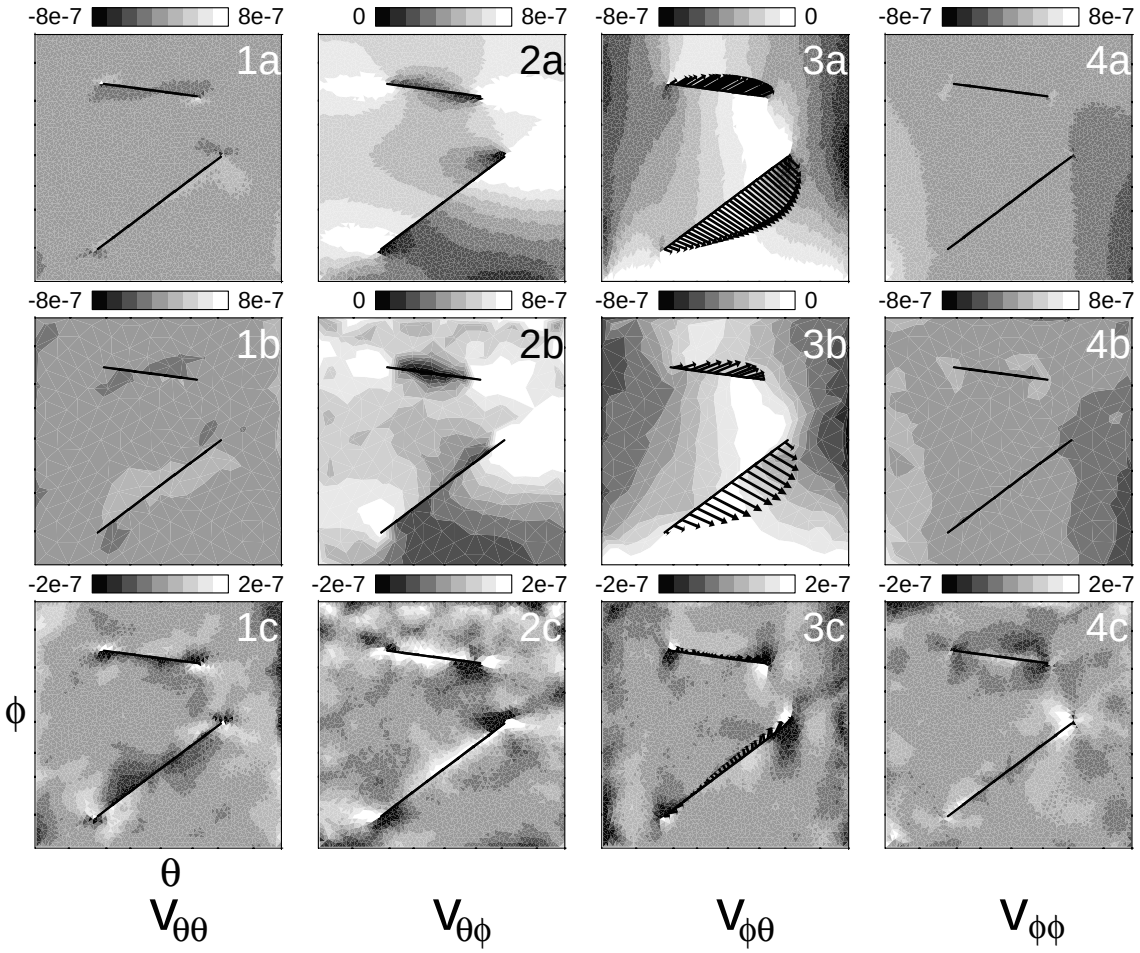

Fig. 7. Difference between model misfit $\boldsymbol{\delta p}_m$ and model error σ_m for each of the components of $\boldsymbol{\nabla v}$ of the selected solution $\boldsymbol{m}$ determined on grid P3. The contouring denotes $\|\delta \boldsymbol{p}_\mu\| - \sigma_m$, only if this difference is larger than zero. Otherwise the value plotted is set to zero.

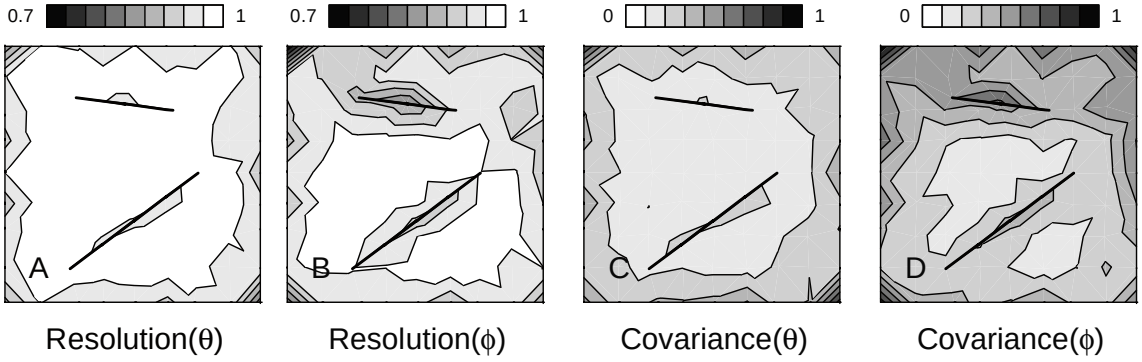

Fig. 8. The diagonal elements R_{ii} of the resolution kernel $\boldsymbol{R}$: (a, b), and C_{ii} of the covariance $\boldsymbol{C}$: (c, d) for components of $\boldsymbol{\nabla v}$. The spatial resolution for $v_{\theta\theta}$ and $v_{\phi\theta}$ (a) and for $v_{\theta\phi}$ and $v_{\phi\phi}$ (b) are the same. Similarly for the covariance (c) and (d). The covariance is scaled by a factor of $1{\cdot}10^{-14}$.

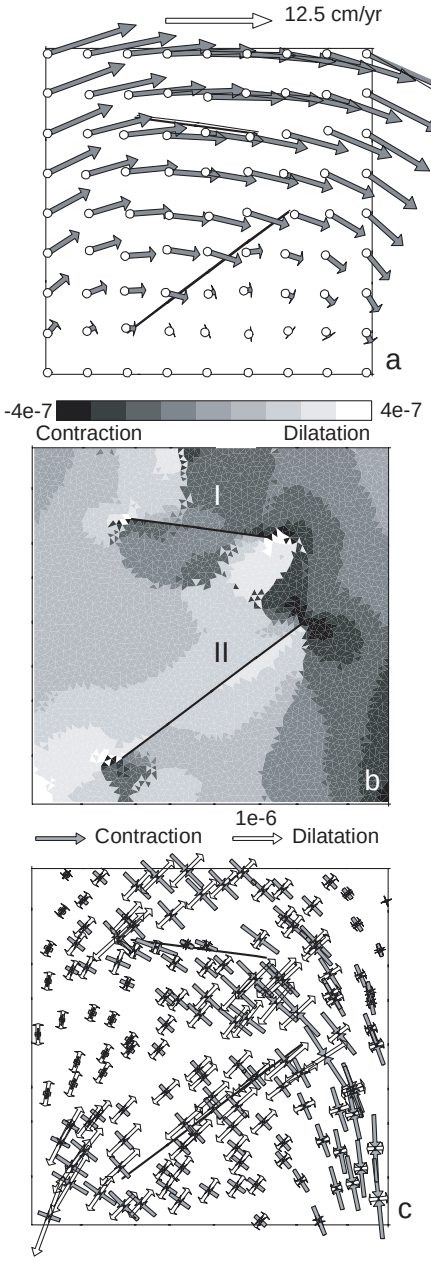

Fig. 2. A synthetic model computed with 6238 finite elements and generated by application of a shear stress to the top boundary. The bottom boundary is kept fixed. The top, left and right boundaries are free to deform. (a) Velocity field computed at 81 observation points; (b) Contoured effective strain rate field ($\pm\sqrt{\frac{1}{2}\dot{\epsilon}\dot{\epsilon}}$). The discontinuous transitions in the contouring result from our choice to add a minus sign to the effective strain rate in case contraction dominates in amplitude. (c) Principal strain rates at 150 arbitrary locations. The two black lines represent the two frictionless faults.

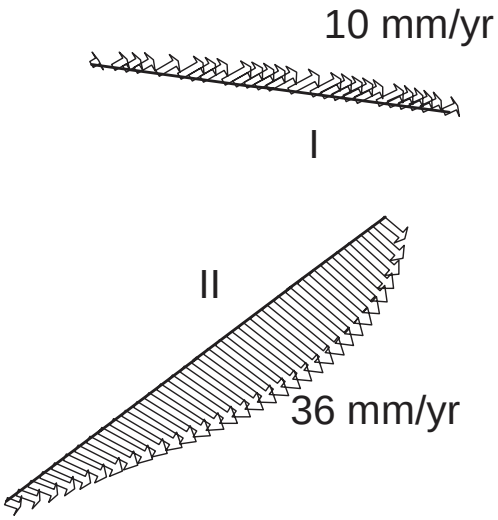

Fig. 3. The distribution of fault motion, denoted by slip vectors, on faults I and II (see figure 2b). Fault I accommodates right-lateral normal slip rates on 26 splitted nodes with a maximum of about 10 mm/yr at the center. Fault II is a right-lateral thrust with 32 splitted nodes and with a maximal slip rate of about 36 mm/yr.

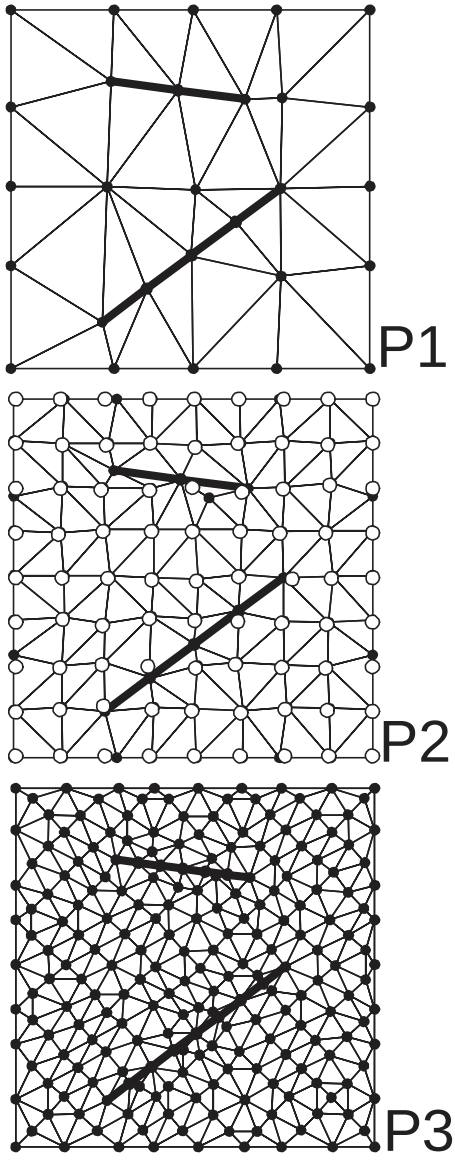

Fig. 4. Three grids P1, P2, and P3 defining different detail of model parameterization. Grid P1 consists of 38 triangles and 14 fault segments; grid P2 consists of 134 triangles and 14 segments (the white dots indicate the 81 station positions which almost all coincide with model nodes); grid P3 consists of 394 triangles and 28 fault segments.

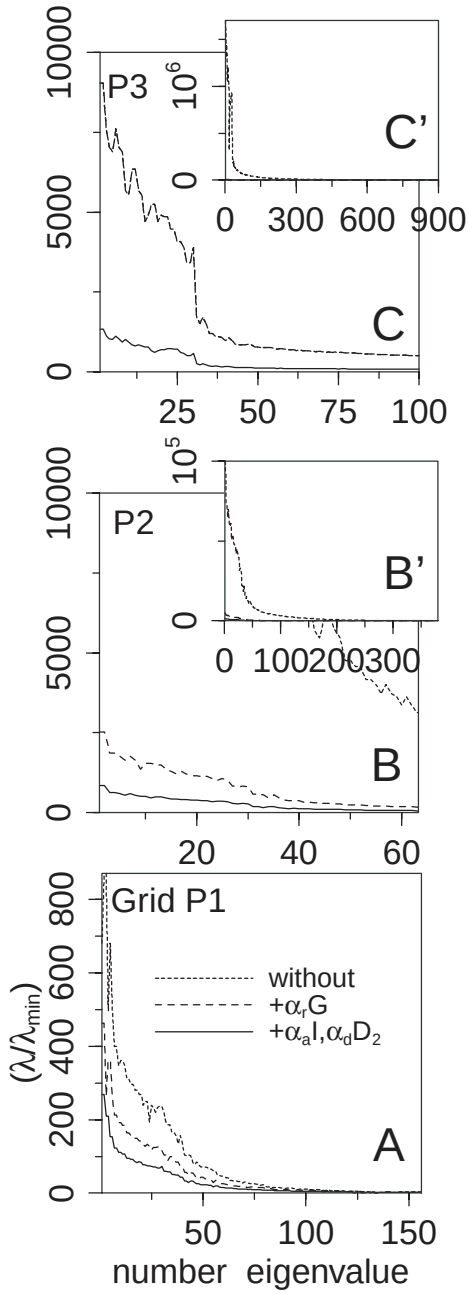

Fig. 5. Eigenvalue spectra of $\boldsymbol{C}^{-1}$ (normalized by the smallest eigenvalue) pertaining to inversions on grids P1, P2 and P3. Key: dotted line, $\sigma_r = \alpha_a = \alpha_d = 0$; dashed line, $\sigma_r = \sigma_r^\mu$, $\alpha_a = \alpha_d = 0$; solid line, $\sigma_r = \sigma_r^\mu$, $\alpha_a = \alpha_a^\mu$ and $\alpha_d = \alpha_d^\mu$ (see table 1); (A), (B') and (C') display the complete spectra, (B) and (C) show the first part of (B') and (C'), respectively.

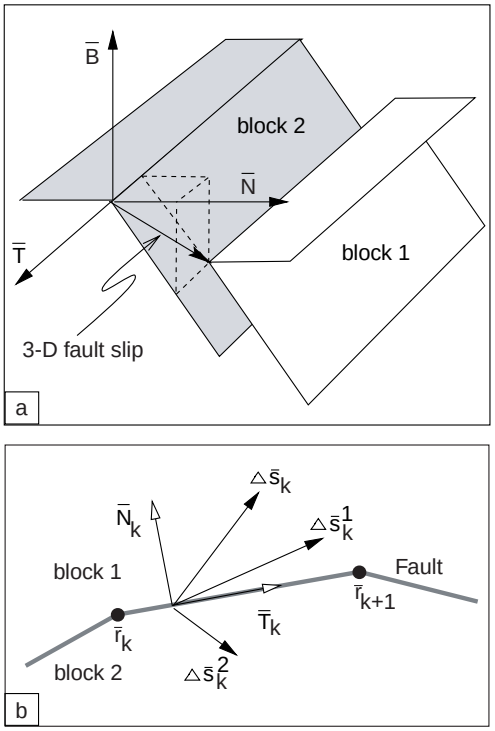

Fig. 9. Illustration of the parameterization of 3-D fault slip. a) Two crustal blocks that have experienced a 3-D relative displacement and the triad of unit vectors $\boldsymbol{T}$, $\boldsymbol{N}$, $\boldsymbol{B}$ used for the definition of fault segments. b) Map view of a fault between "block 1" and "block 2" at fault segment k and horizontal unit vectors indicated. Also denoted are the absolute (horizontal) block displacements $\Delta \boldsymbol{s}_k^1$, and $\Delta \boldsymbol{s}_k^2$, and the relative displacement $\Delta \boldsymbol{s}_k$.